Methylene blue-covered superparamagnetic iron oxide nanoparticles combined with red light as a novel platform to fight non-local bacterial infections: A proof of concept study against *Escherichia coli*

Victor Hladkyi Toledo[a], Tania Mateus Yoshimura[b], Saulo Toledo Pereira[b], Carlos Eduardo Castro[c], Fabio Furlan Ferreira[c], Martha Simões Ribeiro[b], Paula Silvia Haddad[a],*

[a] *Department of Chemistry, Federal University of São Paulo (UNIFESP), 09961-400 Diadema, SP, Brazil*
[b] *Center for Laser and Applications, Energy and Nuclear Research Institute (IPEN), 05508-000 São Paulo, SP, Brazil*
[c] *Center for Natural and Human Sciences (CCNH), Federal University of ABC (UFABC), 09210-580 Santo André, SP, Brazil*

ARTICLE INFO

ABSTRACT

Currently, antimicrobial photodynamic therapy (APDT) is limited to the local treatment of topical infections, and a platform that can deliver the photosensitizer to internal organs is highly desirable for non-local ones; SPIONs can be promising vehicles for the photosensitizer. This work reports an innovative application of methylene blue (MB)-superparamagnetic iron oxide nanoparticles (SPIONs). We report on the preparation, characterization, and application of MB-SPIONs for antimicrobial photodynamic therapy. When exposed to light, the MB photosensitizer generates reactive oxygen species (ROS), which cause irreversible damage in microbial cells. We prepare SPIONs by the co-precipitation method. We cover the nanoparticles with a double silica layer – tetra-ethyl orthosilicate and sodium silicate – leading to the hybrid material magnetite-silica-MB. We characterize the as-prepared SPIONs by Fourier transform infrared spectroscopy, powder X-ray diffraction, and magnetic measurements. We confirm the formation of magnetite using powder X-ray diffraction data. We use the Rietveld method to calculate the average crystallite size of magnetite as being 14 nm. Infrared spectra show characteristic bands of iron-oxygen as well as others associated with silicate groups. At room temperature, the nanocomposites present magnetic behavior due to the magnetite core. Besides, magnetite-silica-MB can promote ROS formation. Thus, we evaluate the photodynamic activity of Fe_3O_4-silica-MB on *Escherichia coli*. Our results show the bacteria are completely eradicated following photodynamic treatment depending on the MB release time from SPIONs and energy dose. These findings encourage us to explore the use of magnetite-silica-MB to fight internal infections in preclinical assays.

1. Introduction

The study of nanostructured systems has allowed new light-based therapeutic approaches, *e.g.*, antimicrobial photodynamic therapy (APDT), to fight infectious diseases [1]. Superparamagnetic iron oxide nanoparticles (SPIONs) have been attracting great attention of the scientific community due to their biomedical applications [2–7]. Owing to their reduced dimensions, iron oxide nanoparticles (NPs), in particular, magnetite (Fe_3O_4) and maghemite (γ-Fe_2O_3), present important features including superparamagnetic behavior and high saturation

magnetization. Consequently, these NPs can be directed to target sites using an external magnetic field [8,9], besides being much less toxic than their correlative materials [10–12]. Another advantage of these NPs is their large surface to volume ratio [13], which allows the functionalization of therapeutic molecules on their surface [14–16]. The NP surface can be tailored with targeting agents or functional groups to change their physical or biological properties. Therefore, adapted arrangement, configuration, structure, morphology, and size of magnetic NPs are critical parameters to determine their efficiency for biomedical applications [17–19]. Several molecules can be used to functionalize the SPIONs' surface [12,15,20]. Among them, an important method to attach SPIONs with therapeutic molecules involves the use of silica, which prevents agglomeration and oxidation of magnetite iron ions [21,22]. Silica is a stable material that can act both as a matrix and a delivery agent for molecules of interest [23–25].

Antimicrobial photodynamic therapy uses photosensitizer (PS) molecules to inactivate microbial cells. When exposed to light, the PS goes to its excited singlet state. By intersystem crossing, the PS can decay for its triplet state, and transfer either charge to the substrate or energy to molecular oxygen to produce highly reactive oxygen species (ROS), as hydroxyl radical, anion superoxide, hydrogen peroxide and singlet oxygen ($^1O_2$), which damage microbial cells by oxidative stress [26].

Mainly, methylene blue (MB) is a cost-effective PS that holds remarkable photochemical and photophysical characteristics [27] to promote photodynamic killing of cancer and microbial cells [28–31]. Additionally, MB is commercially available, and it has been carefully used for several years in other clinical applications [32,33]. Currently, MB-mediated APDT is a powerful strategy to combat infectious diseases [34–36]. Due to its action on multiple targets, there are no reports about the selection of resistant microorganisms to APDT [37]. However, APDT is still limited to the topical treatment of superficial infections due to the difficulty of photosensitizer delivery into internal organs. Envisaging novel APDT applications, in this work, we develop a methylene blue magnetic nanocarrier as a potential vehicle dedicated to fighting internal infectious diseases by APDT [16,25,38–40].

Herein, we obtained Fe_3O_4 NPs by the co-precipitation of iron(II) and iron(III) salts in aqueous solution. NPs were covered with MB-entrapped silica. The obtained NPs were characterized by powder X-ray diffraction (PXRD), Fourier transform infrared spectroscopy (FTIR), scanning electron microscopy (SEM) with energy dispersive X-ray fluorescence spectrometry (EDS), dynamic light scattering (DLS), and SQUID magnetic measurements. Indirect kinetic measurements of $^1O_2$ release from NPs were also performed. Posteriorly, we evaluated the photodynamic inactivation (PDI) of Fe_3O_4-silica-MB on *Escherichia coli* (*E. coli*)), a Gram-negative bacterium responsible for many common infectious diseases, including gastrointestinal tract infections, considering the MB release time from SPIONs and energy dose. Our results demonstrate the possible use of MB-entrapped silica-coated Fe_3O_4 NPs for APDT.

2. Materials and Methods

2.1. Materials

Iron(II) chloride tetrahydrate ($FeCl_2.4H_2O$), iron(III) chloride hexahydrate ($FeCl_3.6H_2O$), ammonium hydroxide (NH_4OH), tetraethylammonium chloride (TEA), methylene blue (MB), tetraethyl orthosilicate (TEOS), sodium silicate (Na_2SiO_3), 1,3-diphenylisobenzofuran (DPBF) were acquired from Sigma Aldrich, USA. Ethanol, sodium chloride (NaCl) and potassium chloride (KCl) were purchased from LabSynth, Brazil. Disodium hydrogen phosphate (Na_2HPO_4) was purchased from Merck, Germany. Potassium dihydrogen phosphate (KH_2PO_4) was purchased from Greentec, Brazil. Brain heart infusion broth was purchased from HiMedia, India. All chemicals were used as received. Analytical grade water from a

Millipore Milli-Q Gradient filtration system was used to prepare the aqueous solutions.

3. Methods

3.1. Synthesis of superparamagnetic iron oxide NPs

The NPs were synthesized by the co-precipitation method [41] from a mixture of iron(II) and iron(III) solution under magnetic stirring and base addition. Specifically, 8 mL of $FeCl_3 \cdot 6H_2O$ solution (1 mol L^{-1}) and 2 mL of $FeCl_2 \cdot 4H_2O$ solution (2 mol L^{-1}) were prepared by dissolving the iron chlorides in hydrochloric acid (HCl) 2 mol L^{-1}. These solutions were mixed and stirred by a magnetic stirrer under the addition of 200 mL ammonium chloride (NH_4OH) 0.7 mol L^{-1} leading to the formation of a dark precipitate, typical of Fe_3O_4 NPs formation. The precipitate was magnetically decanted by a neodymium-iron-boron (Nd-Fe-B) magnet and washed six times with Milli-Q water for non-magnetic residue removal. After washing and isolating the SPIONs, the solid was dispersed in 110 mL of Milli-Q water, and to this dispersion, we added 12 mL of TEA [16] (0.4 mol L^{-1}); this mixture was stirred for 10 min, magnetically decanted and washed six times with ethanol.

3.2. Synthesis of MB-containing silica-coated superparamagnetic iron oxide NPs

For the first silica coating, TEA-containing Fe_3O_4 NPs were suspended in 40 mL of Na_2SiO_3 0.1 mol L^{-1} and stirred for 2 h leading to the formation of Fe_3O_4-SiO_2 NPs, that were magnetically decanted and washed six times with ethanol. After Fe_3O_4-SiO_2 NPs isolation and drying, 0.3 g of the solid was suspended in 20 mL of Milli-Q water and put under sonication for 10 min. The suspension was added in 65 mL of MB (Sigma Aldrich, ≥ 82% purity) 6.15 mmol L^{-1} dissolved in ethanol, and to this mixture, we added 1 mL of TEOS and 3 mL of NH_4OH (27%). The solution was magnetically stirred for 24 h in the dark, generating NPs with two silica layers functionalized with MB (Fe_3O_4-$2SiO_2$-MB). The product was magnetically decanted and washed 4 times with 40 mL of ethanol, and the supernatant was reserved for posterior functionalization efficiency characterization.

3.3. Powder X-ray diffraction (PXRD)

Powder X-ray diffraction data (Fe_3O_4, Fe_3O_4-SiO_2, and Fe_3O_4-$2SiO_2$-MB) were collected (in transmission mode) on a STADI-P diffractometer (Stoe®, Darmstadt, Germany), operating at 50 kV and 40 mA, at room temperature, using $MoK\alpha_1$ radiation (λ = 0.7093 Å). The samples were mounted in a spinning sample holder, and data were recorded by a Mythen 1 K detector (Dectris®, Baden, Switzerland) in the range from 5.000° to 66.605° (2θ) with a step size of 0.015° (2θ) and an integration time of 100 s at each 0.785°.

3.4. Fourier transform infrared (FT-IR) spectroscopy

Dry NPs (Fe_3O_4, Fe_3O_4-SiO_2, and Fe_3O_4-$2SiO_2$-MB) were put together with potassium bromide (KBr) powder using a 1:100 *w/w* sample: ratio. The samples were hand-ground into fine powders, pelleted in a mechanical press and analyzed using an FTIR 630 from Agilent. Single Reflection Diamond ATR for use with the Cary 630. The background was obtained by using a pure KBr pellet. The FT-IR spectra were recorded from 400 to 4000 cm^{-1} at a resolution of 4 cm^{-1}.

3.5. The efficiency of MB functionalization on the NP surface

The efficiency of MB loading on the NPs surface was measured with the UV–Vis method. Briefly, free MB was removed from the NPs by ultracentrifugation. The amount of free MB was determined based on the MB absorbance band at 654 nm (ε = 74.901 mol L^{-1} cm^{-1}) [16] in

a UV–Vis spectrophotometer (model 8553, Agilent, USA). We used the Beer's law to calculate the concentration of residual MB. Therefore, the quantity of MB charged on the NPs was calculated from the charging efficiency (*CE*) equation:

$$CE(\%) = \left(\frac{total_{MB} - residual_{MB}}{total_{MB}} \right) \times 100 \tag{1}$$

3.6. Scanning electron microscopy (SEM) and energy dispersive X-ray fluorescence spectrometry (EDS)

EDS and SEM images were acquired using a JSM-6610LV microscope (JOEL). The powdered samples (Fe_3O_4-SiO_2 and Fe_3O_4-2SiO_2-MB) were deposited into carbon tapes and metalized with gold for analysis with an energy dispersive X-ray fluorescence spectrometry (EDS) module. The EDS technique was utilized for the semi-quantitative and qualitative microanalysis of the sample elements and chemical mapping of the NPs surface.

3.7. Magnetic properties

Magnetization measures were carried out using a superconducting quantum interference device (SQUID) magnetometer (model MPMS XL7, Quantum Design, USA) at 300 K. The dried samples were loaded in Lucite sample holders.

3.8. Hydrodynamic size, size distribution, and zeta potential

The DLS measurements were carried out using an ALV/CGS-3 (ALV-GmbH, Langen, Germany) compact goniometer system equipped with a 22 mW HeNe linearly polarized laser ($\lambda = 633$ nm), a digital correlator (ALV 7004) and a pair of avalanche photodiodes operating in the pseudo-cross-correlation mode. The measurements were performed at (25 ± 1) °C, with the samples loaded in 10-mm-diameter glass cells. An angular range of 90° was set to obtain the autocorrelation functions, which were adjusted with the cumulant method. The NPs' average zeta potentials (ζ) were obtained utilizing electrophoretic light scattering (ELS) measurements using a Zetasizer Nano-ZS ZEN3600 equipment (Malvern Instruments, UK).

3.9. Kinetics of $^1O_2$ generation

The compound used to monitor the generation of $^1O_2$ in the spectrophotometer was *p*-nitrosodimethylaniline (p-NDA), with absorption wavelength at 440 nm, which undergoes a secondary reaction (bleaching) with an intermediate formed through the primary reaction between histidine (His) and singlet oxygen as exemplified in the following reaction [42]:

$$^1O_2 + His \rightarrow [HisO_2]$$

$$[HisO_2] + p - NDA \rightarrow Colorless\ product$$
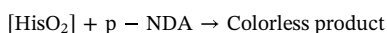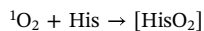
To perform the kinetics, all the following solutions were prepared in 0.01 mol L^{-1} phosphate-buffered saline (PBS) solution with pH adjusted to 7.2: 0.03 mol L^{-1} histidine solution, 25 µmol L^{-1} p-NDA solution, 150 µmol L^{-1} MB solution and a suspension of Fe_3O_4-2SiO_2-MB 1.15 mg mL^{-1}, sonicated for 10 min. Then, three kinetic measurements were performed under different conditions. In the first experimental condition, PBS solution, histidine solution, and the Fe_3O_4-2SiO_2-MB suspension in 1:1:1 volume ratio was placed in a quartz cuvette as the blank. The blank was recorded as soon as the particles were put in suspension since they tend to precipitate quickly due to their high concentration. The kinetics was then performed for 6 min with a 1-s interval in the dark and under continuous resuspension of the particles with a Pasteur pipette. The test in the dark was performed only to confirm the impossibility of a parallel reaction leading to p-NDA

bleaching in the absence of light. In the second experimental condition, the blank was prepared as aforementioned. The kinetics, in this case, was performed in the same conditions as above, except for the fact it was irradiated with a white light-emitting diode (LED) during the kinetics time, to evaluate the generation of $^1O_2$ by Fe_3O_4-2SiO_2-MB. To compare pure MB and Fe_3O_4-2SiO-MB nanosystem as a $^1O_2$ generator, the kinetics was also performed with a pure MB 50 µmol L^{-1} solution. The blank solution was prepared by mixing PBS, histidine, and MB solutions in a 1:1:1 volume ratio. After blank recording, the sample for the kinetics was prepared by mixing histidine solution, p-NDA solution, and MB solution 150 µmol L^{-1} in a 1:1:1 volume ratio. Time and light conditions for singlet oxygen generation were the same as those used in previous cases. Once kinetics was finished, and the p-NDA decay curve is obtained, the compound and singlet oxygen concentrations over time can be calculated through a calibration curve for p-NDA [42].

3.10. Kinetics of MB release

A 58 µg mL^{-1} Fe_3O_4-2SiO_2-MB aqueous dispersion was prepared and placed in a quartz cuvette to measure the spontaneous release of MB without any additional process. Absorbance values were collected for 24 h with measurements at every 1 s at $\lambda = 610$ nm, which is the maximum absorbance of MB released by Fe_3O_4-2SiO_2-MB.

3.11. Photodynamic inactivation

Escherichia coli cells (ATCC 33694) were cultivated in brain heart infusion (BHI) broth for 20 h at 36 °C to use them in an exponential growth phase. Cells were gathered by swab and posteriorly suspended in phosphate buffer saline (PBS). Suspensions of 10^7 colony-forming units per milliliter (CFU mL^{-1}) were settled at spectrophotometer (SP220, Biospectro, Brazil) at an optical density of 0.022 at 600 nm and standardized for PDI assays. After that, cells were incubated with Fe_3O_4-2SiO_2 or Fe_3O_4-2SiO_2-MB solutions at room temperature at 3 different release times of MB: 6, 12, and 22 h. Aliquots of 1000 µL were harvested from each group, placed in a 6-well plate and illuminated with a homemade LED source at $\lambda = (625 \pm 20)$ nm (optical power of 235 mW and irradiance of 16.2 mW cm^{-2}) placed over an orbital shaker. The LED tip was positioned perpendicularly to the wells to guarantee uniform illumination. Four test groups were assessed: I) **Control**, without irradiation, II) **L**, only LED illumination; III) **Fe_3O_4-2SiO_2**, only NPs; IV) **Fe_3O_4-2SiO_2-MB**, entrapped-MB in silica-covered NPs. NPs were used at a concentration of 0.3795 mg mL^{-1}. Besides investigating PDI on *E. coli* depending on the release time of MB from SPIONs, we evaluated 4 different exposure times (5, 10, 15, and 20 min) delivering radiant exposures of 4.86, 9.72, 14.58 and 19.44 J cm^{-2}, respectively. After treatment, we collected aliquots of 20 µL of the suspension and serially diluted in 180 µL of PBS until dilution of 10^{-5} times the original concentration. 10 µL of each dilution were streaked on BHI plates in triplicate using a multichannel pipette. After that, plates were incubated for 20 h at 36 °C to achieve CFU mL^{-1} values.

4. Results and Discussion

Many different novel cancer therapeutic approaches have been explored in the literature; there are already therapies that couple photo-active molecules with nanoparticles that are capable of responding to light [43]. SPIONs were chosen in this work since they exhibit super-paramagnetic behavior when the temperature is raised above the blocking temperature (BT), acting as a single magnetic domain. Such individual nanoparticle has a high magnetic moment and behaves like a giant paramagnetic atom, quickly responding to applied magnetic fields with negligible residual magnetism and coercivity. Magnetic fields are non-invasive and have excellent human tissue penetration. Therefore, iron oxide nanoparticles have been used to activate drug delivery into

the region of interest through an external magnetic field. Besides, the MB anchored on the NPs surface guarantees that the full dose will be delivered to the target. The main subject of this study is to take advantage of the magnetic feature of these nanoparticles as potential vehicles for the methylene blue photoactive molecule.

4.1. Synthesis of Fe_3O_4-SiO_2 and Fe_3O_4-$2SiO_2$-MB

SPIONs can be obtained by different routes [12,44]. The co-precipitation method is generally used due to its simplicity and low cost [45–48]. The NPs can be obtained – at room temperature and atmospheric pressure – with size, morphology, and distribution control of water-dispersed NPs [12]. The co-precipitation takes place with ferrous and ferric ions upon the addition of ammonium hydroxide in aqueous solution (Eq. 2)

$$Fe^{2+}_{(aq)} + 2Fe^{3+}_{(aq)} + 8OH^-_{(aq)} \rightarrow Fe_3O_{4(s)} + 4H_2O_{(l)} \qquad (2)$$
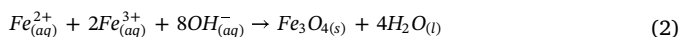
Uncoated particles tend to aggregate in aqueous dispersion; therefore, it is essential the addition of a coating layer on NPs surface to increase their dispersion in water, and their biocompatibility in a biological environment. Silica is a stable and versatile material that can be obtained with shape and size control to carry and deliver drugs [23,24]. Also, grafted on the NPs surface, it stabilizes the NPs. For example, for maghemite particles, silica decreases the transition efficiency to the antiferromagnetic form – α-Fe_2O_3 – with an increase in temperature [49,50]. It also represents a coordination site to functionalize molecules of interest, such as the photoactive molecule MB.

We prepared iron oxide NPs and coated them with silica-containing MB by the *sol-gel* method. The pre-coating is based on the coverage of the as-synthesized NPs surface with Na_2SiO_3, followed by the growth of a second silica layer by condensation of tetraethyl orthosilicate (TEOS) in the presence of the photoactive drug MB [16]. The magnetic core of the NPs was prepared by co-precipitation of iron salts followed by the addition of a weak base (ammonium hydroxide). The suspension formed was magnetically separated, and the NPs were covered with tetraethylammonium (TEA). We then covered these NPs with two silica layer precursors: sodium silicate and TEOS, since the silica layers act as matrices for MB entrapment (Fig. 1). This method is practical, controllable, and generates water-dispersible NPs.

The MB loading efficiency was found to be (90.7 ± 0.3) % for Fe_3O_4-$2SiO_2$-MB, resulting in NPs with 0.28 g of MB per gram of functionalized NPs. This result demonstrates that MB was successfully entrapped on a silica porous matrix layer over a magnetic core composed of SPIONs [16].

4.2. Powder X-ray diffraction (PXRD)

Fig. 2a-c shows the Rietveld plots of the Fe_3O_4, Fe_3O_4-SiO_2, and Fe_3O_4-$2SiO_2$-MB samples, respectively. It is seen at low angles (below 15°) the background of samples Fe_3O_4-SiO_2 and Fe_3O_4-$2SiO_2$-MB displays a hump at ~10.6° (2θ). We utilized the program TOPAS-*Academic* v.6 [51] to perform Rietveld refinements [52] of all samples by taking into account the structural information of magnetite (Fe_3O_4; cubic crystal system, space group $Fd\bar{3}m$) (ICSD card # 26410) [53]. We fitted the background using a 5-term Chebyshev polynomial. We modeled the peak profiles with the Fundamental Parameters approach [54]. The
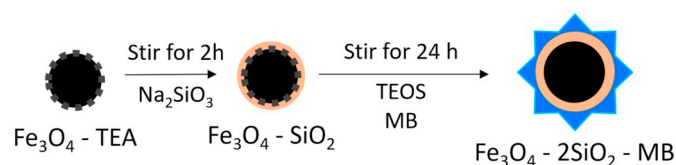

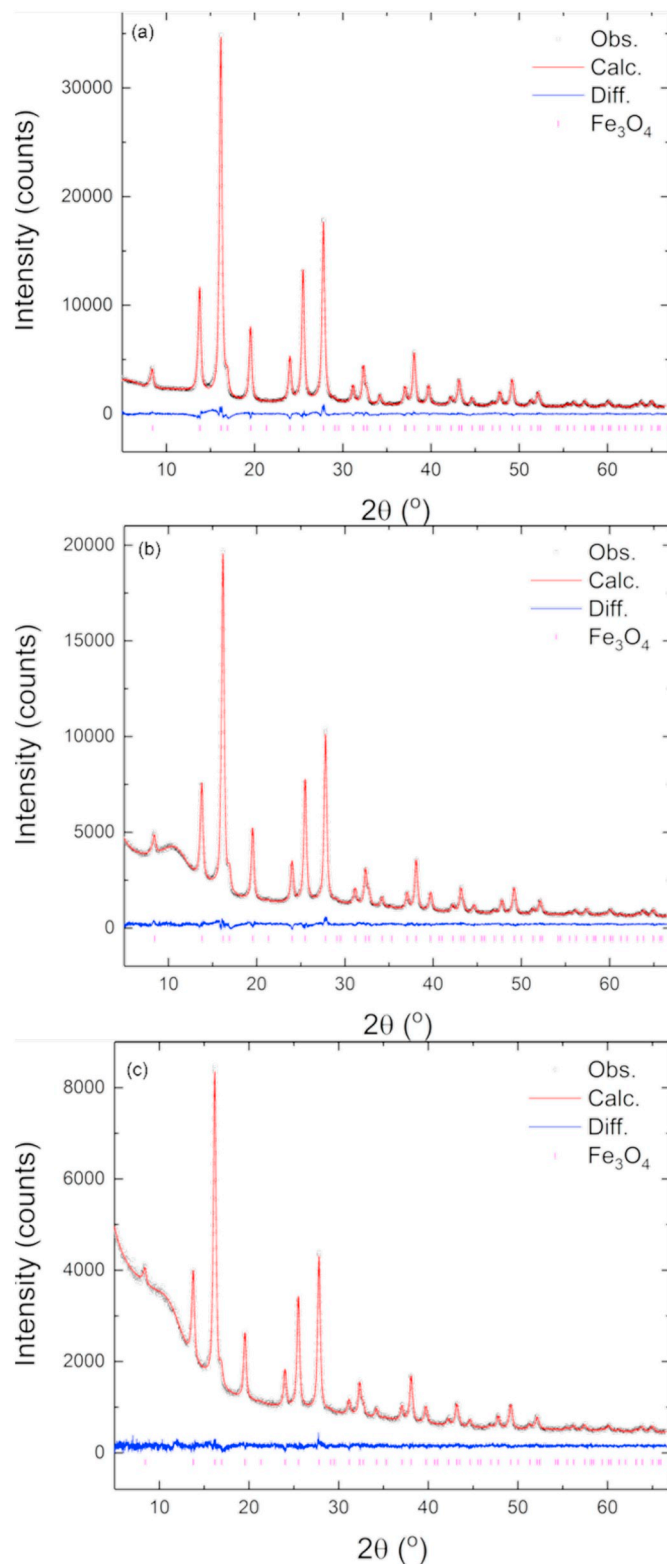**Fig. 1.** Illustrative coating scheme of silica-containing MB on the SPIONs surface.

Fig. 2. Rietveld plots of the (a) Fe_3O_4, (b) Fe_3O_4-SiO_2, and (c) Fe_3O_4-$2SiO_2$-MB samples. The black circles represent the observed patterns, while the red line displays the calculated ones. The blue line indicates the difference between the observed and calculated patterns. The magenta bars stand for the Bragg reflections of magnetite. (For interpretation of the references to colour in this figure legend, the reader is referred to the web version of this article.)
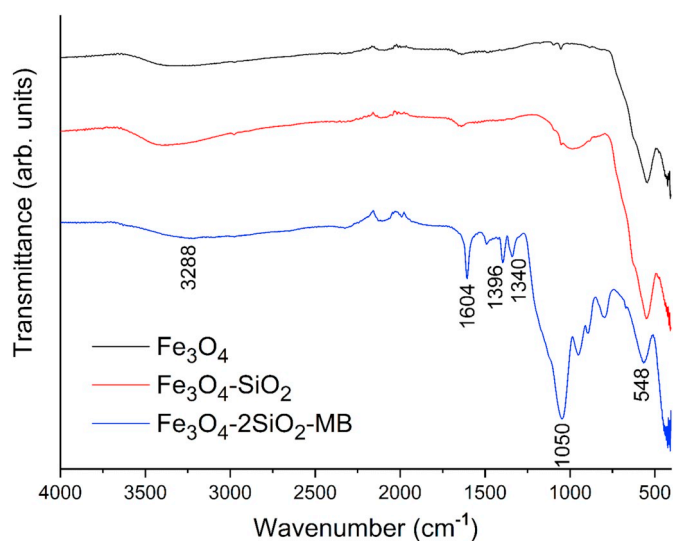
Fig. 3. FT-IR spectra of the Fe_3O_4, Fe_3O_4-SiO_2, and Fe_3O_4-$2SiO_2$-MB samples. The spectra are vertically displaced for better visualization.

isotropic atomic displacements (B_{iso}) were refined independently for each atomic species (Fe^{3+}, Fe^{2+}, and O^{-2}), and the site occupancy of Fe^{2+} ions was refined to infer the vacancies. The last two parameters (B_{iso} and Fe^{2+} vacancy), as well as the unit cell parameters and crystallite size, were all constrained to be equal for the three samples. The refined unit cell parameter was $a = 8.3472(2)$ Å, and the crystallite size was $D = 10.0(1)$ nm; the Fe^{2+} occupancy was equal to 0.884(2). To account for the increase of the amorphous contribution due to the SiO_2 shell (in the case of Fe_3O_4-SiO_2 sample) and $2SiO_2$-MB (for the Fe_3O_4-$2SiO_2$-MB sample), we calculated the "degree of crystallinity - *DoC*" [55] of the samples and found that it decreases with the addition of a second SiO_2 shell (and MB) to the sample. For the Fe_3O_4-SiO_2 and Fe_3O_4-SiO_2-MB samples, the *DoC* were, respectively, 72.92% and 67.48% (considering the Fe_3O_4 sample as being 100% crystalline).

4.3. FT-IR spectra

Fourier transformed infrared spectroscopy (FT-IR) was used to identify the most important stretching vibrations of the magnetic core and the ligands attached to the NPs surface. Fig. 3 highlights the main bands of Fe_3O_4, Fe_3O_4-SiO_2, and Fe_3O_4-$2SiO_2$-MB samples. Low-intensity peaks assigned to the iron oxide core can be observed at 3288 cm^{-1} (νFeO-H) and 548 cm^{-1} (νFe-O) [56]. It is possible to observe bands associated to the MB molecule at 1340 cm^{-1} (νCN) and 1604 cm^{-1} (νC$=$C$_{aromatic}$), low-intensity bands in the range between 950 cm^{-1} and 1600 cm^{-1} attributed to TEA molecule and bands referring to silica at 1050 cm^{-1} (νSi-O), and to νCH around 1396 cm^{-1}. FT-IR analyses confirm the formation of an iron oxide core and the presence of a silica layer-containing MB.

4.4. Hydrodynamic Size (R_H) and Zeta Potential (ζ)

Dynamic light scattering (DLS) measurements were employed to determine the hydrodynamic size and polydispersity index (μ_2/Γ^2). Electrophoretic light scattering (ELS) was used to determine the zeta potential of the NPs. Quantitative data related to the scattering characterization are given in Table 1.

The presence of an additional silica layer (pre-coating) on the Fe_3O_4 surface in the silica-containing MB increases the hydrodynamic size (from 106 to 126 nm). Moreover, the zeta potential is more negative when there is an extra layer of silica, indicating good colloidal stability for Fe_3O_4-$2SiO_2$-MB NPs. This difference between the NPs in the solid-state and in dispersion is a consequence of the presence of extra hydrate

Table 1
DLS and zeta potential data of iron oxide NPs.

NPs	R_H (nm)	μ_2/Γ^2	ζ (mV)
Fe_3O_4-SiO_2	106 ± 2	0.20 ± 0.03	−28.0 ± 1.5
Fe_3O_4-$2SiO_2$-MB	126 ± 1	0.19 ± 0.02	−39.00 ± 0.12

layers in aqueous media.

4.5. Scanning electron microscopy (SEM) and energy dispersive X-ray fluorescence spectrometry (EDS)

Fig. 4 shows SEM images of (a) Fe_3O_4-SiO_2 and (b) Fe_3O_4-$2SiO_2$-MB samples. In both samples, an almost spherical morphology is observed for NPs.

The elemental analysis was performed with EDS in selected areas of the images from Fig. 4 with high-particle concentration, and the obtained EDS spectra for Fe_3O_4-SiO_2 and Fe_3O_4-$2SiO_2$-MB are shown in Fig. 5a and Fig. 5b, respectively.

In the spectrum of the Fe_3O_4-SiO_2 sample (Fig. 5a), peaks referring to iron, oxygen, and silicon can be seen due to the presence of iron oxide and the silica coating, as well as in the spectrum of Fe_3O_4-SiO_2-MB (Fig. 5b) with a relative increase in intensity for silicon and oxygen peaks due to an additional silica layer that was added to the particle. In Fig. 5b, the sulfur signal appears and can be explained by the presence of functionalized MB around the particle, supporting that functionalization was successfully achieved.

4.6. Magnetic behavior

An important characteristic of magnetic NPs for MB vehicles is the superparamagnetic behavior, acting as a single magnetic domain, at temperatures above the BT [16,45,56,57]. The magnetic characterization of hysteresis curves for Fe_3O_4, Fe_3O_4-SiO_2, and Fe_3O_4-$2SiO_2$-MB samples is shown in Fig. 6. Hysteresis isothermal magnetic data confirmed the superparamagnetic behavior of all NPs. The magnetization curves also expose that the residual magnetizations and coercive forces were found to be zero for the NPs. The observed saturation magnetization (*Ms*) value was 76 emu g^{-1} for TEA-containing Fe_3O_4, at room temperature. These results are consistent with our previous work [58], (*Ms* (Fe_3O_4) = 78 emu g^{-1}), which showed that the addition of a polyethylene glycol (PEG) layer on the surface of Fe_3O_4 increased the saturation magnetization due to the modification of the local electron structure of magnetite, shielding the magnetic core, and the same phenomenon may be happening with the TEA. Upon the addition of an extra non-magnetic layer of silica on the Fe_3O_4-TEA nanoparticle surface, a decrease in the *Ms* value was observed (65 emu g^{-1}), and with two layers of silica, the *Ms* decreases for 43 emu g^{-1}.

4.7. $^1O_2$ Generation from Fe_3O_4-$2SiO_2$-MB

Singlet oxygen release kinetics was evaluated indirectly in a buffered aqueous medium. White light LED irradiation was also required, since MB in the particle undergoes dimerization, absorbing light no more at 660 nm, but at 610 nm. The obtained results showed in Fig. 7 and Fig. 8 are promising since there was significant $^1O_2$ formation by functionalized particles compared to free MB.

We can observe a considerable decay for p-NDA absorption band in Fig. 7 and subsequent release of $^1O_2$, after light irradiation in the solution containing Fe_3O_4-$2SiO_2$-MB suspension and in the solution with free MB. After light irradiation for 5 min, the solution containing p-NDA and histidine did not show significant decay in p-NDA absorption, eliminating the possibility of parallel reactions. The kinetics of singlet oxygen formation in an aqueous solution containing free MB and Fe_3O_4-$2SiO_2$-MB suspension is presented in Fig. 8.

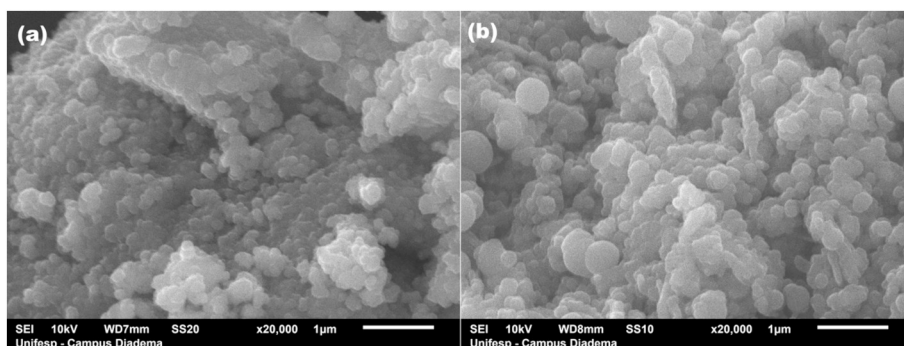**Fig. 4.** SEM images of Fe_3O_4-SiO_2 (a) and Fe_3O_4-$2SiO_2$-MB (b).
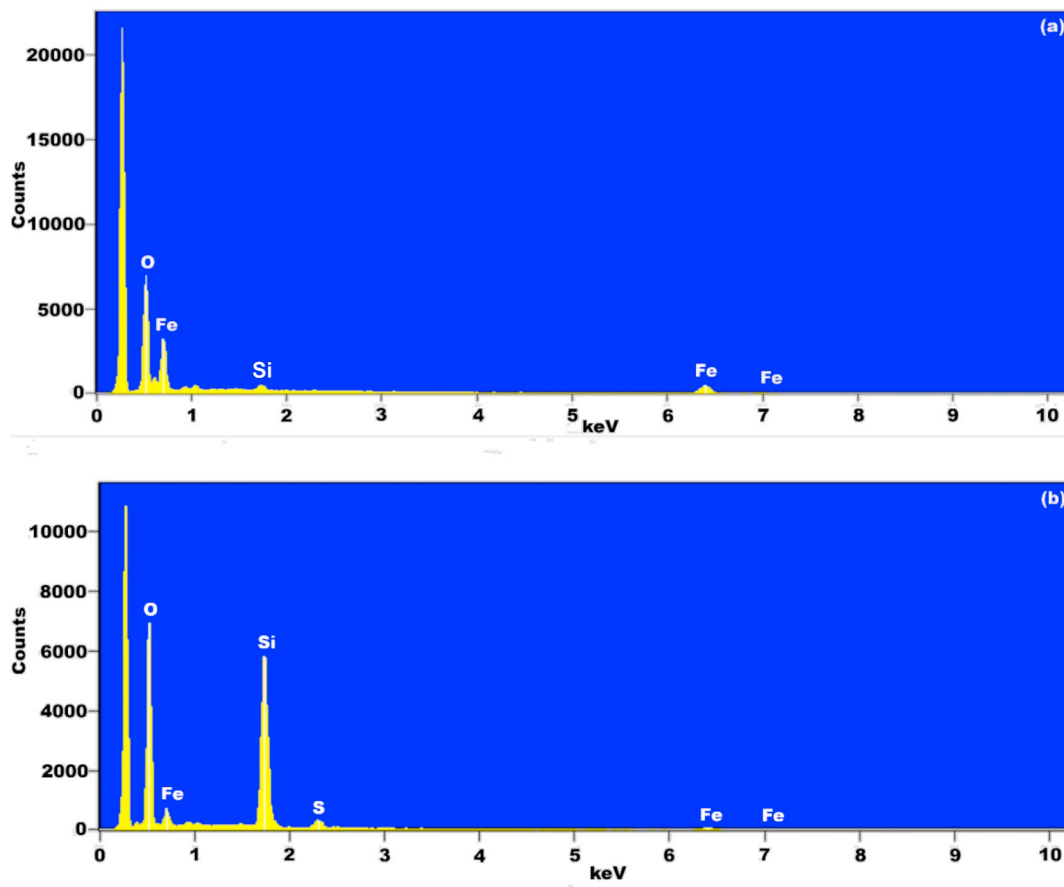

Fig. 5. EDS spectrum of the (a) Fe_3O_4-SiO_2 and (b) Fe_3O_4-SiO_2-MB samples.

In the kinetics, shown in Fig. 8, it is possible to observe the similarity in $^1O_2$ generation by free MB and by Fe_3O_4-$2SiO_2$-MB in higher concentration. In this way, we could evaluate the singlet oxygen release by photosensitizing NPs in PBS, analogous to the biological medium, which was promising due to the proximity with the value for singlet oxygen generated by free MB in a concentration of 50 μmol L^{-1}, with already demonstrated antibacterial effect [59].

4.8. Kinetics of MB release

The kinetic curve of MB release by Fe_3O_4-$2SiO_2$-MB is displayed in Fig. 9. It is worth noting that in the first 2 h, no significant MB liberation was observed. After 2 h, MB concentration starts growing exponentially until it reaches a plateau around 18 h after beginning the kinetics. This result shows that functionalized NPs allows controlled liberation of MB, avoiding the premature release of the photosensitizer

by NPs and its spreading through the biological system, which could lead to side effects or a decrease in treatment efficiency.

4.9. Photodynamic inactivation of E. coli by SPIONs-2SiO$_2$-MB

Fig. 10 exhibits the Fe_3O_4-$2SiO_2$-MB-mediated photodynamic activity on *E. coli*. Interestingly, we can notice that bacterial killing following PDI depends on the time of MB release from NPs and energy dose. If MB is not released (0 h, Fig. 10a), less than 1 log inactivation can be observed after 20 min of irradiation. Following 6 h of MB release, the higher the energy, the higher the bacterial killing; the highest dose promoted about 5 logs inactivation (Fig. 10b). Twelve hours after the MB release, a more pronounced killing was observed after 10 min of irradiation but similar to what was observed after 20 min when compared to the 6 h MB release. After 22 h of MB release, once again, a dose-response curve can be perceived, with complete eradication
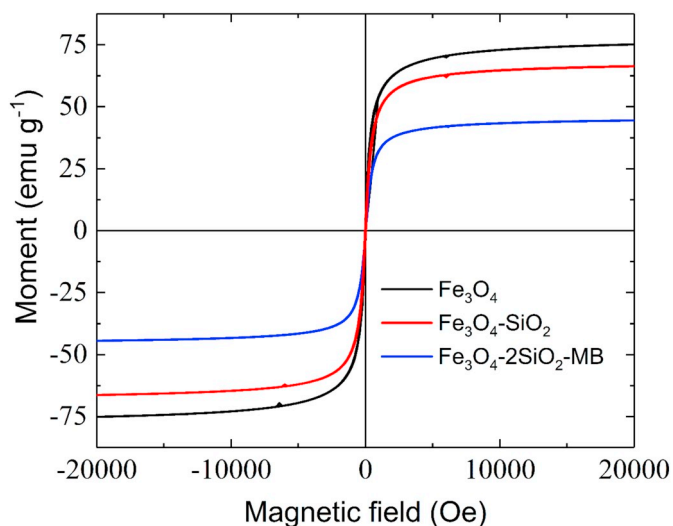
Fig. 6. Magnetic curves of Fe_3O_4; Fe_3O_4-SiO_2 and Fe_3O_4-$2SiO_2$-MB NPs at 300 K.
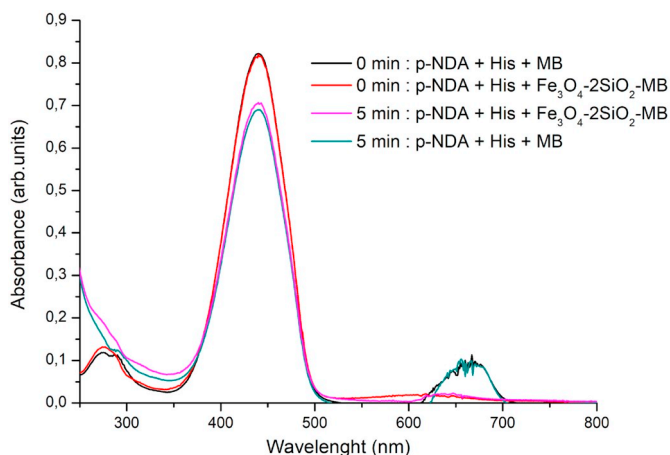

Fig. 7. p-NDA solution absorption spectra with different compositions and irradiation times.
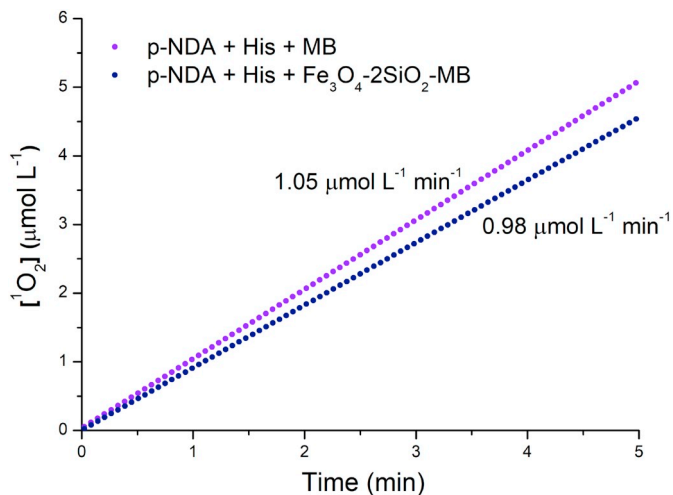

Fig. 8. Kinetics of singlet oxygen formation dependent on the irradiation time.

following 20 min of irradiation. No significant killing was observed for control, LED, and Fe_3O_4-$2SiO_2$ groups. A control MB group was not evaluated since our purpose is to use SPIONs as nanocarriers for MB.
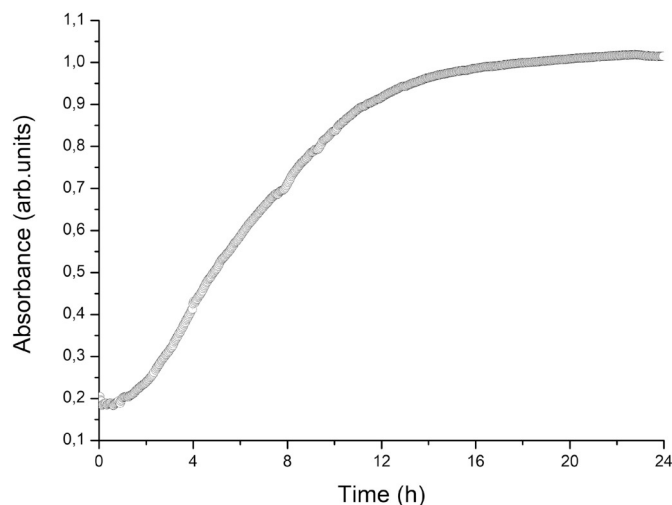

Fig. 9. Kinetics curve of methylene blue liberation by Fe_3O_4-$2SiO_2$-MB. (For interpretation of the references to colour in this figure legend, the reader is referred to the web version of this article.)

Besides, a recent article reported the inactivation kinetics of *E. coli* following MB-mediated APDT [60].

Summarizing, this work is a first attempt to demonstrate that MB-SPIONs can mediate APDT. We hope our findings encourage researchers to pursue the treatment of internal infectious diseases *in vivo*. In this case, the drug could be administered orally or by inhalation from 6 to 22 h before irradiation. MB-SPIONs can be directed to the infected organ in the presence of an external magnetic field applied over the target. Recently, Britos and coworkers reported that SPIONs are good candidates as nanocarriers in biomedical applications using a murine model [58]. Although some previous works in the literature [5,15,61] have shown that SPIONs coated with biocompatible molecules present no significant cytotoxicity to healthy and cancerous cells in low concentrations, the cytotoxicity against mammalian cells had not been evaluated with the MB-coated nanoparticles, and this information could be obtained in future works. Regarding the light source, commercially available devices have already been developed to irradiate cavities such as bladder, esophagus, lung, and stomach, commonly used in cancer PDT. Thus, we envisage a promising nanoplatform to fight infections within the body.

5. Conclusions

We successfully synthesized Fe_3O_4, Fe_3O_4-SiO_2, and Fe_3O_4-$2SiO_2$-MB samples. Powder X-ray diffraction data revealed we obtained Fe_3O_4, and the average crystallite size for all samples was 10.0(1) nm, and the Fe^{2+} occupancy was equal to 0.884(2). The degree of crystallinity for Fe_3O_4-SiO_2 and Fe_3O_4-SiO_2-MB samples were, respectively, 72.92% and 67.48%. We assigned the most important stretching vibrations of the magnetic core and the ligands attached to the NPs surface (TEA, silica, and MB), thus showing the NPs coverage was effectively achieved. The larger hydrodynamic size seen for the Fe_3O_4-$2SiO_2$-MB in comparison to the former Fe_3O_4-SiO_2 sample indicated a second layer was deposited, and MB was entrapped on it. Also, excellent colloidal stability was observed for the Fe_3O_4-$2SiO_2$-MB sample. SEM images revealed the particles have an almost spherical shape, and EDS data showed the presence of sulfur in the Fe_3O_4-$2SiO_2$-MB system, thus indicating the presence of MB. Magnetic measurements displayed a high saturation magnetization for the Fe_3O_4-TEA sample (M_s = 76 emu g^{-1}), with decreasing values due to the addition of subsequent layers of SiO_2 (M_s = 65 emu g^{-1}) and SiO_2-MB (M_s = 43 emu g^{-1}). Singlet oxygen release kinetics was evaluated indirectly in a buffered aqueous medium. A significant amount of $^1O_2$ formation was observed for the
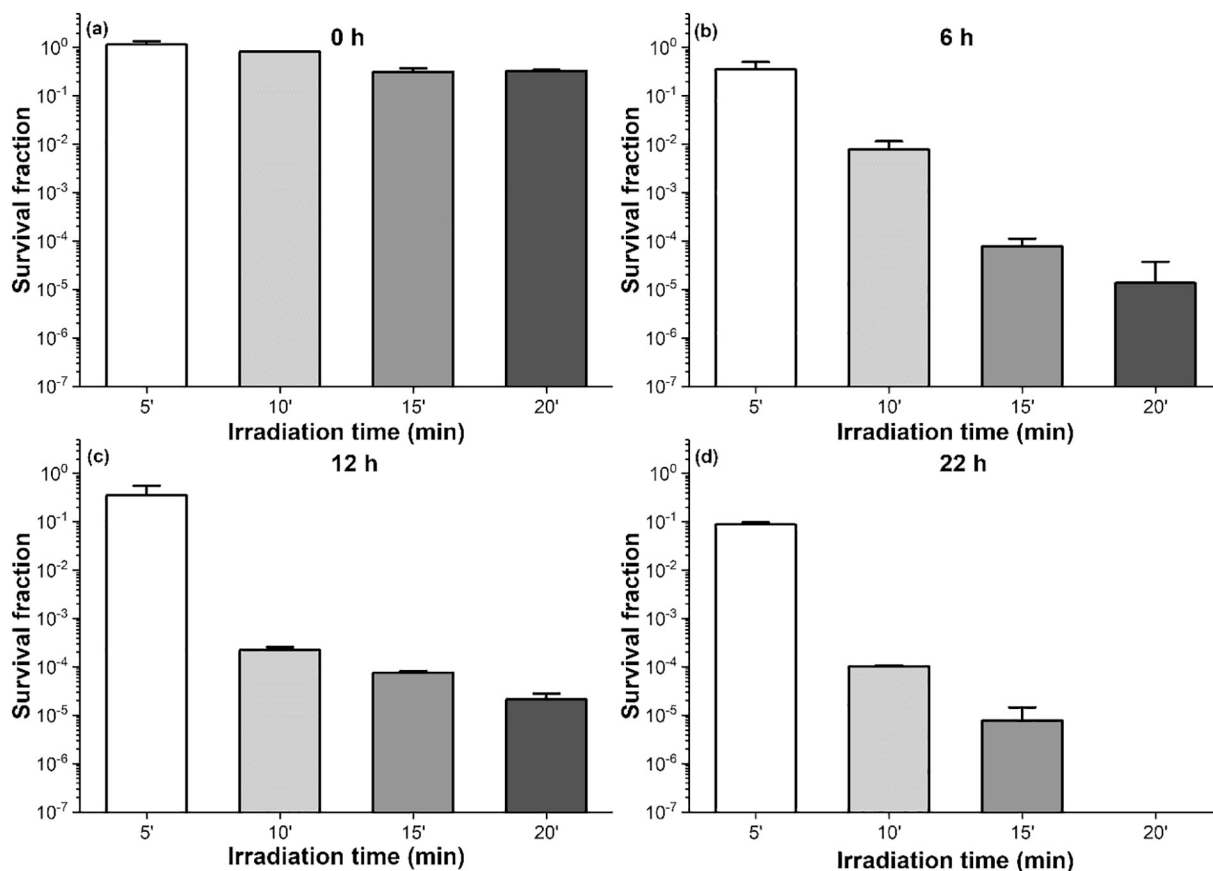
Fig. 10. Mean values ± standard deviation of *E. coli* survival fraction following Fe_3O_4-$2SiO_2$-MB-mediated PDI. (a) no MB release; (b) after 6 h of MB release; (c) after 12 h of MB release; (d) after 22 h of MB release.

functionalized particles when compared to free MB. The MB started being released after 2 h of the kinetics experiment, thus indicating we could avoid a premature release of the photosensitizer. *In vitro* experiments showed that after 22 h of MB release, complete eradication of *E. coli* was achieved following 20 min of irradiation. In fact, *in vitro* assays have shown MB-SPIONs exhibit high potential for PDT application once they present antimicrobial properties. At present, antimicrobial PDT is restricted to local applications, and with SPIONs, one can provide treatment of internal organs.

Author contributions

The manuscript was written through the contributions of all authors. All authors have given approval of the final version of the manuscript.

Declarations of Competing Interest

The authors declare that they have no known competing financial interests or personal relationships that could have appeared to influence the work reported in this paper.

Data availability

The raw/processed data required to reproduce these findings can be shared upon request.

Author Statement

The manuscript was written through contributions of all authors. All authors have given approval to the final version of the manuscript.

Declaration of Competing Interest

The authors declare no competing financial interests.

Acknowledgments

References

[1] R. Yin, T. Agrawal, U. Khan, G.K. Gupta, V. Rai, Y.Y. Huang, M.R. Hamblin, Antimicrobial photodynamic inactivation in nanomedicine: small light strides against bad bugs, Nanomedicine. 10 (2015) 2379–2404, https://doi.org/10.2217/nnm.15.67.

[2] J. Chomoucka, J. Drbohlavova, D. Huska, V. Adam, R. Kizek, J. Hubalek, Magnetic nanoparticles and targeted drug delivering, Pharmacol. Res. 62 (2010) 144–149, https://doi.org/10.1016/j.phrs.2010.01.014.

[3] A.K. Gupta, M. Gupta, Synthesis and surface engineering of iron oxide nanoparticles for biomedical applications, Biomaterials. 26 (2005) 3995–4021, https://doi.org/10.1016/j.biomaterials.2004.10.012.

[4] Q.A. Pankhurst, J. Connolly, S.K. Jones, J. Dobson, Applications of magnetic nanoparticles in biomedicine, J. Phys. D. Appl. Phys. 36 (2003) R167–R181, https://doi.org/10.1088/0022-3727/36/13/201.

[5] A.B. Seabra, T. Pasquôto, A.C.F. Ferrarini, M.D.C. Santos, P.S. Haddad, R. De Lima, Preparation, characterization, cytotoxicity, and genotoxicity evaluations of thiolated- and S-nitrosated superparamagnetic iron oxide nanoparticles: implications for cancer treatment, Chem. Res. Toxicol. 27 (2014) 1207–1218, https://doi.org/10.1021/tx500113u.

[6] M. Saeed, W. Ren, A. Wu, Therapeutic applications of iron oxide based nanoparticles in cancer: basic concepts and recent advances, Biomater. Sci. 6 (2018) 708–725, https://doi.org/10.1039/C7BM00999B.

[7] A.C. Anselmo, S. Mitragotri, A review of clinical translation of inorganic

nanoparticles, AAPS J. 17 (2015) 1041–1054, https://doi.org/10.1208/s12248-015-9780-2.

[8] P. Gajalakshmi, M.K. Priya, T. Pradeep, J. Behera, K. Muthumani, S. Madhwanti, U. Saran, S. Chatterjee, Breast cancer drugs dampen vascular functions by interfering with nitric oxide signaling in endothelium, Toxicol. Appl. Pharmacol. 269 (2013) 121–131, https://doi.org/10.1016/j.taap.2013.03.011.

[9] X. Cai, C. Wang, B. Chen, W. Hua, F. Shen, L. Yu, Z. He, Y. Shi, Y. Chen, G. Xia, J. Cheng, W. Bao, Y. Zhang, X. Wang, Antitumor efficacy of DMSA modified Fe 3 O 4 magnetic nanoparticles combined with arsenic trioxide and Adriamycin in Raji cells, J. Biomed. Nanotechnol. 10 (2014) 251–261, https://doi.org/10.1166/jbn.2014.1787.

[10] U. Schwertmann, R.M. Cornell, Iron Oxides in the Laboratory: Preparation and Characterization, (2000).

[11] J. Sangeetha, J. Philip, Synthesis, characterization and antimicrobial property of Fe3O4-Cys-HNQ nanocomplex, with l-cysteine molecule as a linker, RSC Adv. 3 (2013) 8047, https://doi.org/10.1039/c3ra00005b.

[12] P. Silvia Haddad, A. Barozzi Seabra, Biomedical applications of magnetic nanoparticles, in: Iron oxides Struct, Prop. Appl. (2012) 165–177.

[13] M.E. Davis, Z.G. Chen, D.M. Shin, Nanoparticle therapeutics: an emerging treatment modality for cancer, Nat. Rev. Drug Discov. 7 (2008) 771–782, https://doi.org/10.1038/nrd2614.

[14] A. Masoudi, H.R. Madaah Hosseini, M.A. Shokrgozar, R. Ahmadi, M.A. Oghabian, The effect of poly(ethylene glycol) coating on colloidal stability of superparamagnetic iron oxide nanoparticles as potential MRI contrast agent, Int. J. Pharm. 433 (2012) 129–141, https://doi.org/10.1016/j.ijpharm.2012.04.080.

[15] M.C. Santos, A.B. Seabra, M.T. Pelegrino, P.S. Haddad, Synthesis, characterization and cytotoxicity of glutathione- and PEG-glutathione-superparamagnetic iron oxide nanoparticles for nitric oxide delivery, Appl. Surf. Sci. 367 (2016) 26–35, https://doi.org/10.1016/j.apsusc.2016.01.039.

[16] K.A. Fudimura, A.B. Seabra, M.C. Santos, P.S. Haddad, Synthesis and characterization of methylene blue-containing silica-coated magnetic nanoparticles for photodynamic therapy, J. Nanosci. Nanotechnol. 17 (2017) 133–142, https://doi.org/10.1166/jnn.2017.12715.

[17] K. Ulbrich, K. Holá, V. Šubr, A. Bakandritsos, J. Tuček, R. Zbořil, Targeted drug delivery with polymers and magnetic nanoparticles: covalent and noncovalent approaches, release control, and clinical studies, Chem. Rev. 116 (2016) 5338–5431, https://doi.org/10.1021/acs.chemrev.5b00589.

[18] S. Laurent, D. Forge, M. Port, A. Roch, C. Robic, L. Vander Elst, R.N. Muller, Magnetic iron oxide nanoparticles: synthesis, stabilization, vectorization, physicochemical characterizations and biological applications, Chem. Rev. 108 (2008) 2064–2110, https://doi.org/10.1021/cr068445e.

[19] M. Colombo, S. Carregal-Romero, M.F. Casula, L. Gutierrez, M.P. Morales, I.B. Boehm, J.T. Heverhagen, D. Prosperi, W.J. Parak, ChemInform abstract: biological applications of magnetic nanoparticles, ChemInform 43 (2012), https://doi.org/10.1002/chin.201235272 no-no.

[20] P.S. Haddad, T.N. Britos, L.M. Li, L.D.S. Li, Preparation, characterization and tests of incorporation in stem cells of Superparamagnetic Iron oxide, J. Phys. Conf. Ser. 617 (2015), https://doi.org/10.1088/1742-6596/617/1/012002.

[21] A. Pourjavadi, Z.M. Tehrani, N. Mahmoudi, The effect of protein corona on doxorubicin release from the magnetic mesoporous silica nanoparticles with polyethylene glycol coating, J. Nanopart. Res. 17 (2015), https://doi.org/10.1007/s11051-015-3008-3.

[22] S. Shahbazi, X. Wang, J.L. Yang, X.C. Jiang, R. Ryan, A.B. Yu, Synthesis and surface modification of magnetic nanoparticles for potential applications in sarcomas, J. Nanopart. Res. 17 (2015), https://doi.org/10.1007/s11051-015-3065-7.

[23] A.M. Fales, H. Yuan, T. Vo-Dinh, Silica-coated gold Nanostars for combined SERS detection and singlet oxygen generation: a potential Nanoplatform for Theranostics, Langmuir. 27 (2011) 12186–12190, https://doi.org/10.1021/la202602q.

[24] C. Li, Y. Li, J. Bai, X. Ge, G. Li, C. Su, Z. Yang, Release behavior of methylene blue dimers from silica-methylene blue@octacalcium phosphate powders in phosphate-buffered saline and lysosome-like buffer, J. Sol-Gel Sci. Technol. 75 (2015) 397–406, https://doi.org/10.1007/s10971-015-3712-6.

[25] D.B. Tada, L.L.R. Vono, E.L. Duarte, R. Itri, P.K. Kiyohara, M.S. Baptista, L.M. Rossi, Methylene blue-containing silica-coated magnetic particles: a potential magnetic carrier for pHotodynamic therapy, Langmuir. 23 (2007) 8194–8199, https://doi.org/10.1021/la700883y.

[26] M.S. Baptista, J. Cadet, P. Di Mascio, A.A. Ghogare, A. Greer, M.R. Hamblin, C. Lorente, S.C. Nunez, M.S. Ribeiro, A.H. Thomas, M. Vignoni, T.M. Yoshimura, Type I and type II photosensitized oxidation reactions: guidelines and mechanistic pathways, Photochem. Photobiol. 93 (2017) 912–919, https://doi.org/10.1111/php.12716.

[27] H.C. Junqueira, D. Severino, L.G. Dias, M.S. Gugliotti, M.S. Baptista, Modulation of methylene blue photochemical properties based on adsorption at aqueous micelle interfaces, Phys. Chem. Chem. Phys. 4 (2002) 2320–2328, https://doi.org/10.1039/b109753a.

[28] J.P. Tardivo, A. Del Giglio, C.S. De Oliveira, D.S. Gabrielli, H.C. Junqueira, D.B. Tada, D. Severino, R. De Fátima Turchiello, M.S. Baptista, Methylene blue in photodynamic therapy: from basic mechanisms to clinical applications, Photodiagn. Photodyn. Ther. 2 (2005) 175–191, https://doi.org/10.1016/S1572-1000(05)00097-9.

[29] J.P. Tardivo, A. Del Giglio, L.H. Paschoal, M.S. Baptista, New photodynamic therapy protocol to treat aids-related Kaposi's sarcoma, Photomed. Laser Surg. 24 (2006) 528–531, https://doi.org/10.1089/pho.2006.24.528.

[30] A.F. dos Santos, L.F. Terra, R.A.M. Wailemann, T.C. Oliveira, V. de Morais Gomes, M.F. Mineiro, F.C. Meotti, A. Bruni-Cardoso, M.S. Baptista, L. Labriola, Methylene blue photodynamic therapy induces selective and massive cell death in human

[31] I.O.L. Bacellar, T.M. Tsubone, C. Pavani, M.S. Baptista, Photodynamic efficiency: from molecular photochemistry to cell death, Int. J. Mol. Sci. 16 (2015) 20523–20559, https://doi.org/10.3390/ijms160920523.

[32] M. Oz, D.E. Lorke, M. Hasan, G.A. Petroianu, Cellular and molecular actions of methylene blue in the nervous system Murat, Med. Res. Rev. 31 (2009) 93–117, https://doi.org/10.1002/med.20177.

[33] J.P. Tardivo, F. Adami, J.A. Correa, M.A.parecid.S. Pinhal, M.S. Baptista, A clinical trial testing the efficacy of PDT in preventing amputation in diabetic patients, Photodiagn. Photodyn. Ther. 11 (2014) 342–350, https://doi.org/10.1016/j.pdpdt.2014.04.007.

[34] A.M. de Senna, M.M.F. Vieira, R.M. Machado-de-Sena, A.O. Bertolin, S.C. Núñez, M.S. Ribeiro, Photodynamic inactivation of Candida ssp. on denture stomatitis. A clinical trial involving palatal mucosa and prosthesis disinfection, Photodiagn. Photodyn. Ther. 22 (2018) 212–216, https://doi.org/10.1016/j.pdpdt.2018.04.008.

[35] K.F. Grego, M.P.N. de Carvalho, M.P.V. Cunha, T. Knöbl, F.C. Pogliani, J.L. Catão-Dias, S.S. Sant'Anna, M.S. Ribeiro, F.P. Sellera, Antimicrobial photodynamic therapy for infectious stomatitis in snakes: clinical views and microbiological findings, Photodiagn. Photodyn. Ther. 20 (2017) 196–200, https://doi.org/10.1016/j.pdpdt.2017.10.004.

[36] J.P. Tardivo, M. Wainwright, M. Baptista, Small scale trial of photodynamic treatment of onychomycosis in São Paulo, J. Photochem. Photobiol. B Biol. 150 (2015) 66–68, https://doi.org/10.1016/j.jphotobiol.2015.03.015.

[37] F. Cieplik, D. Deng, W. Crielaard, W. Buchalla, E. Hellwig, A. Al-Ahmad, T. Maisch, Antimicrobial photodynamic therapy–what we know and what we don't, Crit. Rev. Microbiol. 44 (2018) 571–589, https://doi.org/10.1080/1040841X.2018.1467876.

[38] M.E. Wieder, D.C. Hone, M.J. Cook, M.M. Handsley, J. Gavrilovic, D.A. Russell, Intracellular photodynamic therapy with photosensitizer-nanoparticle conjugates: Cancer therapy using a 'Trojan horse, Photochem. Photobiol. Sci. 5 (2006) 727–734, https://doi.org/10.1039/b602830f.

[39] M. Nafiujjaman, V. Revuri, M. Nurunnabi, K. Jae Cho, Y.K. Lee, Photosensitizer conjugated iron oxide nanoparticles for simultaneous in vitro magneto-fluorescent imaging guided photodynamic therapy, Chem. Commun. 51 (2015) 5687–5690, https://doi.org/10.1039/c4cc10444g.

[40] L. Li, M. Nurunnabi, M. Nafiujjaman, Y.Y. Jeong, Y.K. Lee, K.M. Huh, A photosensitizer-conjugated magnetic iron oxide/gold hybrid nanoparticle as an activatable platform for photodynamic cancer therapy, J. Mater. Chem. B 2 (2014) 2929–2937, https://doi.org/10.1039/c4tb00181h.

[41] M.M. Molina, A.B. Seabra, M.G. De Oliveira, R. Itri, P.S. Haddad, Nitric oxide donor superparamagnetic iron oxide nanoparticles, Mater. Sci. Eng. C 33 (2013) 746–751, https://doi.org/10.1016/j.msec.2012.10.027.

[42] S. El Mohsni, I. Kraljic, A new method for the detection of singlet oxygen in aqueous solutions, Photochem. Photobiol. 28 (1978) 577–581.

[43] K. Maier-Hauff, F. Ulrich, D. Nestler, H. Niehoff, P. Wust, B. Thiesen, H. Orawa, V. Budach, A. Jordan, Efficacy and safety of intratumoral thermotherapy using magnetic iron-oxide nanoparticles combined with external beam radiotherapy on patients with recurrent glioblastoma multiforme, J. Neuro-Oncol. 103 (2011) 317–324, https://doi.org/10.1007/s11060-010-0389-0.

[44] L.H. Reddy, J.L. Arias, J. Nicolas, P. Couvreur, Magnetic nanoparticles: design and characterization, toxicity and biocompatibility, pharmaceutical and biomedical applications, Chem. Rev. 112 (2012) 5818–5878, https://doi.org/10.1021/cr300068p.

[45] S.H. Hussein-Al-Ali, M.E. El Zowalaty, M.Z. Hussein, B.M. Geilich, T.J. Webster, Synthesis, characterization, and antimicrobial activity of an ampicillin-conjugated magnetic nanoantibiotic for medical applications, Int. J. Nanomedicine 9 (2014) 3801–3814, https://doi.org/10.2147/IJN.S61143.

[46] S. Yoffe, T. Leshuk, P. Everett, F. Gu, Superparamagnetic Iron oxide nanoparticles (SPIONs): synthesis and surface modification techniques for use with MRI and other biomedical applications, Curr. Pharm. Des. 19 (2012) 493–509, https://doi.org/10.2174/138161282130014.

[47] G. Gnanaprakash, S. Mahadevan, T. Jayakumar, P. Kalyanasundaram, J. Philip, B. Raj, Effect of initial pH and temperature of iron salt solutions on formation of magnetite nanoparticles, Mater. Chem. Phys. 103 (2007) 168–175, https://doi.org/10.1016/j.matchemphys.2007.02.011.

[48] Z.R. Stephen, F.M. Kievit, M. Zhang, Magnetite nanoparticles for medical MR imaging, Zachary, NIH Public Access. 14 (2011) 330–338, https://doi.org/10.1016/S1369-7021(11)70163-8.

[49] E.M. Moreno, M. Zayat, M.P. Morales, C.J. Serna, A. Roig, D. Levy, Preparation of narrow size distribution superparamagnetic γ-Fe2O3 nanoparticles in a sol-gel transparent SiO2 matrix, Langmuir. 18 (2002) 4972–4978, https://doi.org/10.1021/la020037s.

[50] C. Cannas, M.F. Casula, G. Concas, A. Corrias, D. Gatteschi, A. Falqui, A. Musinu, C. Sangregorio, G. Spano, Magnetic properties of γ-Fe2O3-SiO2 aerogel and xerogel nanocomposite materials, J. Mater. Chem. 11 (2001) 3180–3187, https://doi.org/10.1039/B104562H.

[51] A.A. Coelho, J. Evans, I. Evans, A. Kern, S. Parsons, The T OPAS symbolic computation system, Powder Diffract. 26 (2011) S22–S25, https://doi.org/10.1154/1.3661087.

[52] H.M. Rietveld, A profile refinement method for nuclear and magnetic structures, J. Appl. Crystallogr. 2 (1969) 65–71, https://doi.org/10.1107/S0021889869006558.

[53] M.E. Fleet, The structure of magnetite, Acta Crystallogr. Sect. B Struct. Crystallogr. Cryst. Chem. 37 (1981) 917–920, https://doi.org/10.1107/S0567740881004597.

[54] R.W. Cheary, A. Coelho, Fundamental parameters approach to x-ray line-profile fitting, J. Appl. Crystallogr. 25 (1992) 109–121, https://doi.org/10.1107/

S0021889891010804.

[55] C.C. Hernandez, F.F. Ferreira, D.S. Rosa, X-ray powder diffraction and other analyses of cellulose nanocrystals obtained from corn straw by chemical treatments, Carbohydr. Polym. 193 (2018) 39–44, https://doi.org/10.1016/j.carbpol.2018.03.085.

[56] R. Kumar, B.S. Inbaraj, B.H. Chen, Surface modification of superparamagnetic iron nanoparticles with calcium salt of poly(γ-glutamic acid) as coating material, Mater. Res. Bull. 45 (2010) 1603–1607, https://doi.org/10.1016/j.materresbull.2010.07.017.

[57] D. Dorniani, A.U. Kura, M.Z. Bin Hussein, S. Fakurazi, A.H. Shaari, Z. Ahmad, Controlled-release formulation of perindopril erbumine loaded PEG-coated magnetite nanoparticles for biomedical applications, J. Mater. Sci. 49 (2014) 8487–8497, https://doi.org/10.1007/s10853-014-8559-7.

[58] T.N. Britos, C.E. Castro, B.M. Bertassoli, G. Petri, F.L.A. Fonseca, F.F. Ferreira, P.S. Haddad, In vivo evaluation of thiol-functionalized superparamagnetic iron oxide nanoparticles, Mater. Sci. Eng. C 99 (2019) 171–179, https://doi.org/10.1016/j.msec.2019.01.118.

[59] F.P. Sellera, C.P. Sabino, M.S. Ribeiro, R.G. Gargano, N.R. Benites, P.A. Melville, F.C. Pogliani, In vitro photoinactivation of bovine mastitis related pathogens, Photodiagn. Photodyn. Ther. 13 (2016) 276–281, https://doi.org/10.1016/j.pdpdt.2015.08.007.

[60] C.P. Sabino, M. Wainwright, C. dos Anjos, F.P. Sellera, M.S. Baptista, N. Lincopan, M.S. Ribeiro, Inactivation kinetics and lethal dose analysis of antimicrobial blue light and photodynamic therapy, Photodiagn. Photodyn. Ther. 28 (2019) 186–191, https://doi.org/10.1016/j.pdpdt.2019.08.022.

[61] P.S. Haddad, T.N. Britos, M.C. Santos, A.B. Seabra, M.V. Palladino, G.Z. Justo, Synthesis, characterization and cytotoxicity evaluation of nitric oxide-Iron oxide magnetic nanoparticles, J. Phys. Conf. Ser. 617 (2015) 1–8, https://doi.org/10.1088/1742-6596/617/1/012022.